

# Constructing Precise Coordination of Nickel Active Sites on Hierarchical Porous Carbon Framework for Superior Oxygen Reduction

HPSTAR  
1229-2021

Shuai Zhang, Hui Xue, Wan-lu Li, Jing Sun, Niankun Guo, Tianshan Song, Hongliang Dong,\* Jiangwei Zhang,\* Xin Ge, Wei Zhang,\* and Qin Wang\*

Single-atom catalysts (SACs) with specific coordination environment are expected to be efficient electrocatalysts for oxygen reduction reaction (ORR). Herein, Ni–N<sub>4</sub>–C<sub>10</sub> coordination site is constructed through encapsulating Ni<sup>2+</sup> into the cavity of ZIF-8 as a self-sacrificing precursor and anchoring it on 3D N-doped carbon frameworks. The Ni–N<sub>4</sub>–C<sub>10</sub> catalyst shows excellent ORR activity and stability, with a high half-wave potential (0.938 V vs RHE), which is currently the best performances in Ni-based SACs. The remarkable performance with high ORR activity in alkaline solution is attributed to the single-atom nickel active sites with faster electron transport and suitable electronic structure. Moreover, the power density of zinc-air battery assembled by Ni–N<sub>4</sub>–C<sub>10</sub> as cathode is 47.1% higher than that of the commercial Pt/C. This work not only provides a facile method to prepare extremely active Ni-based SACs, but also studies the intrinsic mechanism toward the oxygen reduction reaction under alkaline condition.

for solving the slow kinetics for oxygen reduction reaction (ORR).<sup>[2]</sup> Up till now, platinum group metals are still believed to be the most efficient ORR electrocatalyst. However, the applications of the noble catalysts on a large scale are seriously restricted by the cost, stability, and scarcity.<sup>[3]</sup> Thus, the development of efficient Pt-based alternative catalysts for ORR has become a top priority.

Single-atom catalysts (SACs), which could reduce particle size to atomic level and maximize the atom utilization and exposure of active sites, is considered to be beneficial for different electrocatalytic reactions.<sup>[4]</sup> Atomic-scale SACs (M–N–C) have gradually become one of the most prospective candidates for replacing noble metal materials in the field of electrocatalysis.<sup>[5]</sup> In that case, metal–organic

frameworks (MOFs) are defined as an ideal self-sacrificing template for the construction of SACs because of the controllable and confinement effect of cavity.<sup>[6]</sup> Various traditional metal-supported N-doped carbon materials have been developed based on the carbonization of MOFs precursors. Owing to the carbon-nitrogen-rich networks and the flexible cavities that can easily accommodate foreign active transition metals, zeolite

## 1. Introduction

The increasing environmental pollution and energy crisis derived from the use of fossil fuels have prompted to the development of efficient, clean, and sustainable energy, such as metal-air batteries and conductive membrane fuel cells.<sup>[1]</sup> One of the major obstacles is the synthesis of active catalysts

S. Zhang, Dr. H. Xue, J. Sun, N. K. Guo, T. S. Song, Prof. Q. Wang  
College of Chemistry and Chemical Engineering  
Inner Mongolia University  
Hohhot 010021, P. R. China  
E-mail: qinwang@imu.edu.cn

Dr. W.-l. Li  
Chemical Sciences Division, Lawrence Berkeley National Laboratory  
Berkeley, CA 94720, USA

Dr. W.-l. Li  
Kenneth S. Pitzer Center for Theoretical Chemistry  
University of California Berkeley  
Berkeley, CA 94720, USA

Prof. H. L. Dong  
Center for High Pressure Science and Technology Advanced Research  
Shanghai 201203, P. R. China  
E-mail: hongliang.dong@hpstar.ac.cn

Prof. J. W. Zhang  
Dalian National Laboratory for Clean Energy and State  
Key Laboratory of Catalysis  
Dalian Institute of Chemical Physics  
Chinese Academy of Sciences  
Dalian 116023, P. R. China  
E-mail: jwzhang@dicp.ac.cn

Prof. X. Ge, Prof. W. Zhang  
Key Lab of Mobile Materials MOE  
School of Materials Science and Engineering  
and Electron Microscopy Center  
and International Center of Future Science  
Jilin University  
Changchun 130012, P. R. China  
E-mail: weizhang@jlu.edu.cn

 The ORCID identification number(s) for the author(s) of this article can be found under <https://doi.org/10.1002/smll.202102125>.

DOI: 10.1002/smll.202102125

imidazolate frameworks (ZIFs) are generally selected as efficient precursor for preparing M–N–C catalysts.<sup>[7]</sup> Up till now, numerous SACs with diverse transition metal center have been prepared. Most of the reported literatures focused on the effect of central metal atoms on the ORR performance of M–N–C catalysts, and the ORR activity follows the sequence Fe > Co > Cu > Mn > Ni.<sup>[8]</sup> The Ni–N<sub>4</sub> center composed of Ni atom and four N atoms is difficult to form OOH\* owing to its weak ability to bind O and resulting in H<sub>2</sub>O<sub>2</sub> production to hinder 4e<sup>−</sup> process.<sup>[9]</sup> Basically, the ORR activity and stability of SACs is highly determined by the tailoring of first- and second- or higher-coordination shells, and the local coordination environment of the central atom is closely related to its catalytic activity and stability.<sup>[10]</sup> Therefore, by accurately adjusting the coordination electronic structure of Ni–N–C, reducing the energy barrier between the Ni-based center and oxygen and reaction intermediates can accelerate electron transport, thereby improving the oxygen reduction performance. Therefore, the construction of Ni SACs with a Ni–N–C coordination structure is extremely important for greatly improving its ORR activities.

Herein, atomically dispersed Ni–N–C active site, which was anchored on N-doped polyhedral carbon framework, has been in situ developed by calcination of Ni@ZIF-8. The as-obtained Ni–N–C manifests a superior ORR property, as demonstrated by an ultrahigh half-wave potential of 0.938 V, which is the best activity in Ni-based center SACs with Ni–N<sub>4</sub>–C<sub>10</sub> coordination up to now. Density functional theory (DFT) calculations indicated that the suitable adsorption and desorption capabilities for reaction intermediates, and the Ni–N–C active sites possessed higher charge density and faster electron transport efficiency, which could significantly improve the ORR performance. Furthermore, zinc-air battery assembled by Ni–N–C showed a remarkably enhanced property with a power density of 178 mW cm<sup>−2</sup>, which is superior to the commercial Pt/C catalyst. This work offered a facile strategy to develop Ni-based SACs with outstanding ORR performance, and further studied the intrinsic mechanism of SACs under alkaline condition.

## 2. Results and Discussion

As shown in **Figure 1a**, ZIF-8 had been used as sacrifice template to synthesize Ni–N–C catalyst. Ni<sup>2+</sup> was encapsulated into the flexible cavity of ZIF-8 and converted into Ni–N<sub>4</sub> species in situ by one-step pyrolysis. As a contrast, a suite of Ni–N–C samples with different molar ratios of Ni were also developed using the same method. The optimal catalyst was expressed as Ni–N–C (the molar ratio of Ni<sup>2+</sup> was 0.1). In addition, the nitrogen-doped carbon (N–C) without Ni was also obtained by the carbonization of ZIF-8. The transmission electron microscopy (TEM) and scanning electron microscope (SEM) had been carried out to study the particle size and morphology of the obtained electrocatalysts. Obviously, the Ni–N–C and N–C samples retained the rhombic dodecahedron shape of the precursor, and the particle size was about 120 nm, while the evaporation of Zn reduced by carbon matrix at high temperature led to a rougher particle surface (**Figure 1b,c**).<sup>[11]</sup> Meanwhile, the Ni–N–C-0.06, Ni–N–C-0.08, and Ni–N–C-0.12 also maintained the polyhedral structure of ZIF-8 (**Figure S1**,

**Supporting Information**). Next, high-resolution TEM (HRTEM) and nitrogen adsorption-desorption analysis had been selected to evaluate the porous structures of the Ni–N–C and N–C samples (**Figure 1d**; **Figures S2 and S3**, **Supporting Information**). At a low pressure ( $P/P_0 = 0.05–0.06$ ), the volume adsorption of Ni–N–C and N–C samples increased significantly, while at a higher pressure ( $P/P_0 = 0.45–0.95$ ), an obvious hysteresis loop was observed, indicating that both micropore and mesopore existed in these two samples (**Figure S3**, **Supporting Information**). The Brunauer–Emmett–Teller (BET) surface areas and the total pore volume of Ni–N–C were 1305 m<sup>2</sup> g<sup>−1</sup> and 0.937 cm<sup>3</sup> g<sup>−1</sup>, respectively. And these two values were 1466 m<sup>2</sup> g<sup>−1</sup> and 1.053 cm<sup>3</sup> g<sup>−1</sup> for N–C, which may be caused by the evaporation or rare residue of metallic Zn during pyrolysis process (**Figures S3 and S4**, **Supporting Information**).<sup>[12]</sup> With respect to N–C sample, it indicated that Ni–N–C had more distinct porous structures, including micropores and mesopores (**Figure S4**, **Supporting Information**). The specific surface areas of mesopore were 280 and 321 m<sup>2</sup> g<sup>−1</sup> for N–C and Ni–N–C, respectively, indicating the increase of the content of mesopore in Ni–N–C catalyst. Meanwhile, the content of micropore decreased in Ni–N–C, and the specific surface areas were 1217 and 1037 m<sup>2</sup> g<sup>−1</sup> for N–C and Ni–N–C, respectively. The abundant mesopores structure and a large specific surface area would be expected to be beneficial for fast mass transport in the ORR process.<sup>[13]</sup> The High-angle annular dark-field scanning transmission electron microscopy (HAADF-STEM) and elemental mapping verified that the C, N, and Ni were distributed uniformly throughout the dodecahedron of Ni–N–C in **Figure 1e**. **Figure 1f** revealed the isolated bright dots concentrated distributed in the N-doped carbon framework, which proved the existence of Ni single atom. The X-ray diffraction (XRD) patterns were selected to study the crystalline structures of the obtained samples. As can be seen in **Figure 1g**, Ni@ZIF-8 had been prepared successfully. And both N–C and Ni–N–C showed just two peaks at 24° and 42°, which could be attributed to the (002) and (100) of carbon, respectively. The Raman spectra showed two characteristic carbon resonances at 1580 cm<sup>−1</sup> (G-band) and 1350 cm<sup>−1</sup> (D-band), assigning to the graphitic sp<sup>2</sup> carbon and sp<sup>3</sup> carbon, respectively (**Figure S5**, **Supporting Information**).<sup>[14]</sup> The I<sub>D</sub>/I<sub>G</sub> ratio of Ni–N–C is 0.91, lower than that of N–C (0.92), indicating the highly graphitic carbon substrate was obtained in Ni–N–C sample.

The chemical states were tested by using X-ray photoelectron spectroscopy (XPS). The survey spectrum indicated that the Ni, N, C, and O elements could be well observed in the Ni–N–C sample (**Figure 2a**; **Figure S6**, **Supporting Information**). The Ni 2p peak was not detected owing to the low content of Ni (0.18 at%, **Table S1**, **Supporting Information**). And this result matched well with the data derived from inductively coupled plasma atomic emission spectroscopy (ICP-AES) (**Figure 2b**; **Table S2**, **Supporting Information**). The N 1s spectrum indicated the presence of two nitrogen species, including graphitic N (400.9 eV) and pyridinic N (398.5 eV) (**Figure 2c**; **Figure S7**, **Supporting Information**). The pyridinic N species has been demonstrated to be beneficial to the electrocatalytic performance. As can be seen from **Figure 2d**, the binding energy at 284.8 eV can be ascribed to the sp<sup>2</sup> carbon, illustrating that high-quality conjugated honeycomb lattice were obtained.<sup>[15]</sup>

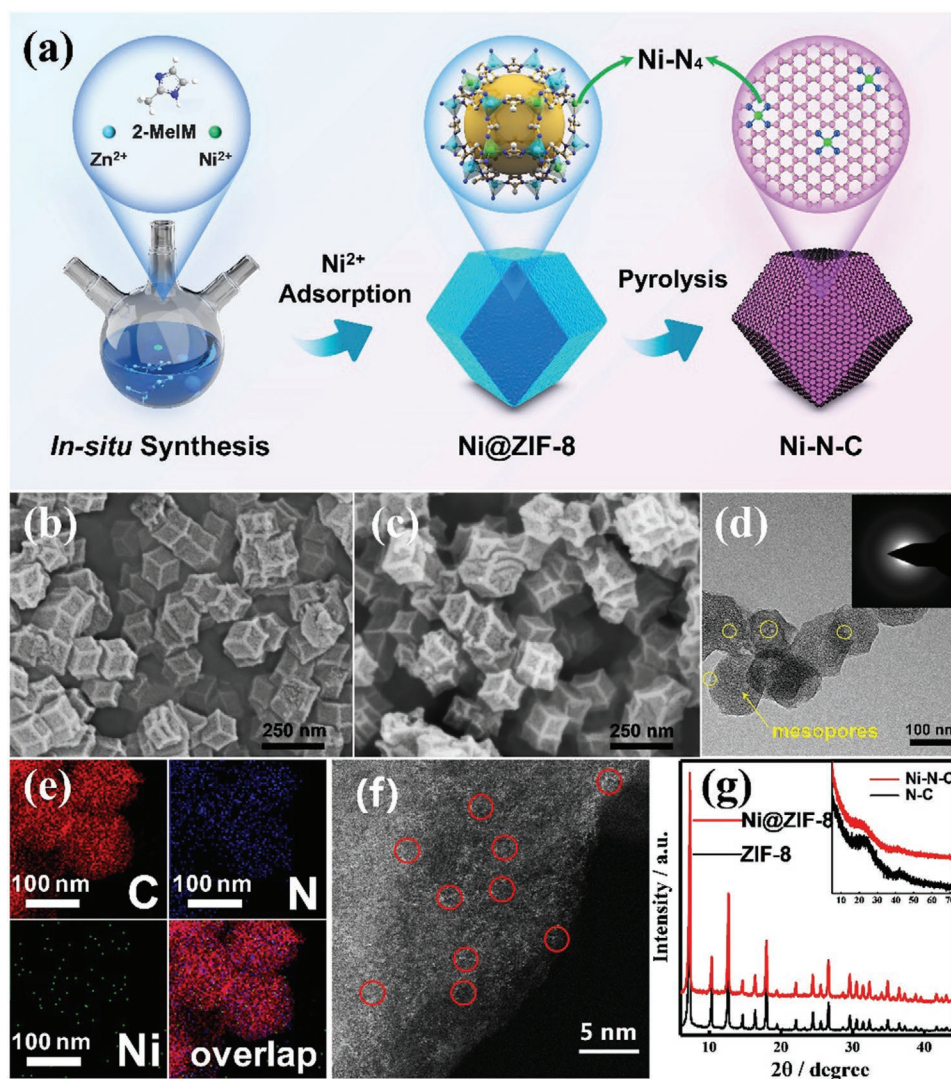


**Figure 1.** a) Schematic procedure for the synthesis of Ni–N–C, b) SEM image of N–C, c) SEM image of Ni–N–C, d) TEM image of Ni–N–C, e) elemental mapping results of Ni–N–C, f) atomic-resolution HAADF-STEM image of Ni–N–C, and g) XRD patterns of ZIF-8, Ni@ZIF-8, and their derivatives.

Other binding energies at 286.1 and 288.7 eV related to carbon had also been detected and can be designed as C–N and C–O groups (Figures S8 and S9, Supporting Information). In addition, the in-deep structural information of Ni–N–C was studied by extended X-ray absorption fine structure (EXAFS). The EXAFS results showed a peak at 1.887 Å, indicating primary Ni–N coordination in Ni–N–C sample (Figure 2e; Table S3, Supporting Information). However, the Ni–Ni peak at 2.45 Å could not be observed from the Ni–N–C catalyst.<sup>[16]</sup> The Ni–N<sub>4</sub> configuration structure could also be found in NiPc (Figure S10, Supporting Information). This result corroborated that the atomic dispersion of Ni–N<sub>4</sub> sites has been formed. In Figure 2f, the X-ray absorption near-edge structure (XANES) spectra of Ni–N–C lied between the Ni foil and NiO, obviously indicated the distinct electronic structure of Ni<sup>δ+</sup> (0 < δ < 2). The white-line intensity of Ni–N–C was higher than that of Ni foil, indicating positively charged state of Ni atoms induced by electron transfer from Ni to the carbon matrix, as commonly

seen in SACs. Compared with NiO, the white-line intensity of Ni–N–C decreases, which indicated that the electronic properties of the single Ni atom had been adjusted.<sup>[17]</sup> Figure S11 (Supporting Information) further shows that average oxidation state of Ni in Ni–N–C is 1.84. On the basis of the fitting results, the local structure of the proposed Ni–N–C was that Ni coordinated with four nitrogen atoms in first shell and ten carbon atoms in second shell to form Ni–N<sub>4</sub>–C<sub>10</sub> coordination (inset in Figure 2f; Figure S12 and Table S3, Supporting Information). EXAFS wavelet transform analysis (W-T) of atomic Ni dispersion was carried out, whose location is highly associated to the path length R (Figure 2g–i; Figure S13, Supporting Information). As shown in Figure 2g, there is no detection of Ni–Ni metal bond similar to Ni foil in Ni–N–C, which indicates the atomic-level dispersion of Ni elements on account of the signal of the second coordination sphere of Ni–N–C is similar to scattering path of phthalocyanine Ni. The bond length of Ni–N–C is significantly different from the Ni–Ni metal bond.

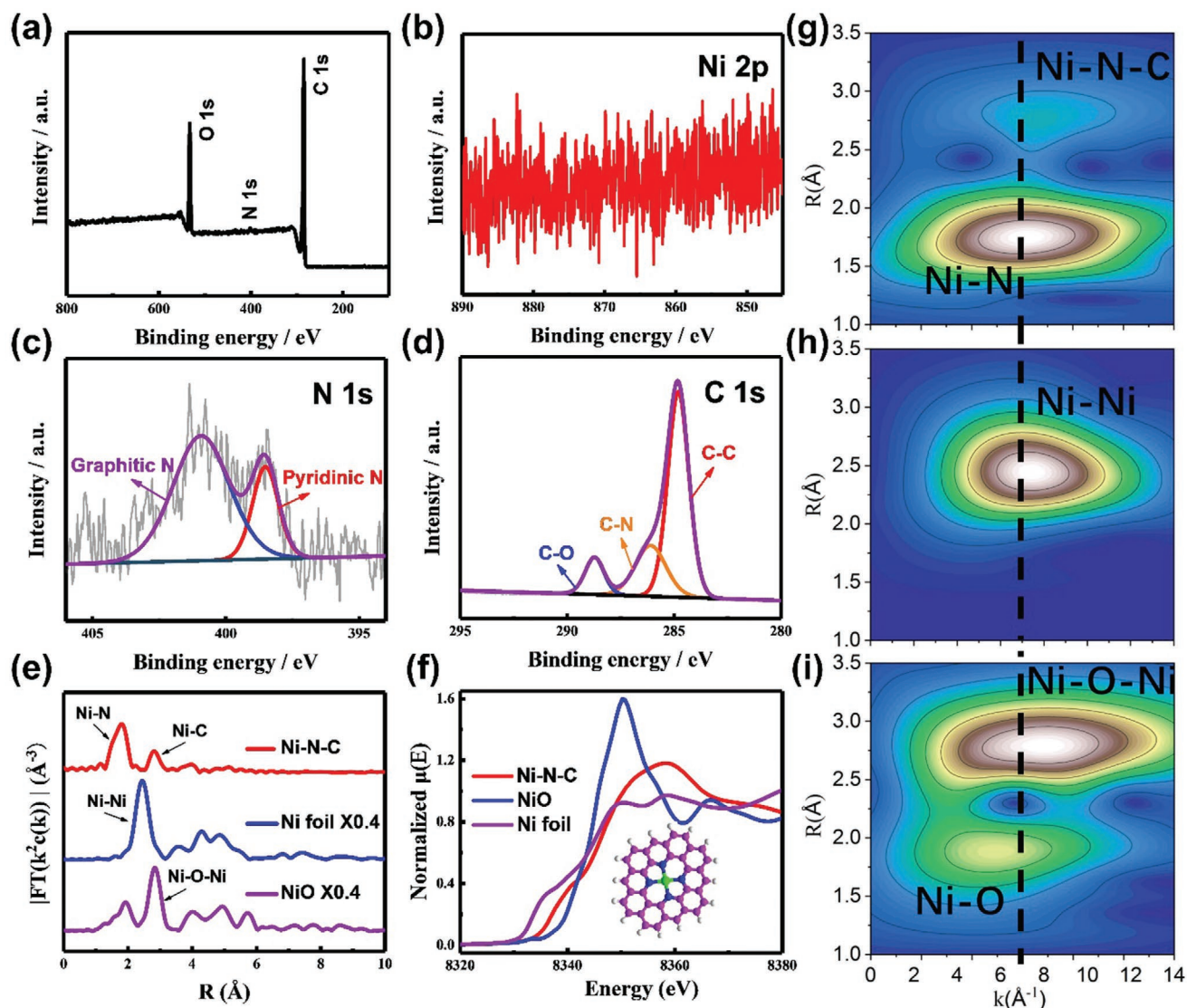


**Figure 2.** XPS spectra of Ni–N–C: a) survey spectra, b) Ni 2p, c) N 1s, and d) C 1s, e) Ni K-edge EXAFS spectrum, f) Ni K-edge XANES spectrum of Ni–N–C, Ni foil, NiO (inset shows schematic structural model for Ni–N–C), Ni K-edge 2D wavelet transform for: g) Ni–N–C, h) Ni foil, and i) NiO, respectively.

The scattering path signal of samples at  $[\chi(k), \chi(R)]$  as shown in Table S4 (Supporting Information). Two scattering path signals including the Ni–N bonds located at  $[6, 1.78]$ . According to re-fitting the second coordination sphere, the phthalocyanine Ni and Ni–N–C have a very similar coordination environment, but the second coordination layer environment is different (Figure S14, Supporting Information). In addition, for the four nitrogen mesoatoms in phthalocyanine Ni and two carbon mesoatoms in Ni–N–C, the coordination environments of the nitrogen species are also significantly different, leading to the differences in the XANES feature peak (Figure 2f). It is a particular type of metal electronic structure combined with a specific type nitrogen to form Ni–N–C catalysts with excellent ORR performance.

The ORR performances of the Ni–N–C were studied based on the rotating disk electrode (RDE) method in 0.1 M

O<sub>2</sub>-saturated KOH solution. For comparison, other comparative catalysts, including the N–C, Ni–N–C-0.06, Ni–N–C-0.08, Ni–N–C-0.12, and the commercial Pt/C (20 wt%) catalysts, were also measured in the same conditions. As seen from Figure 3a,b, the Ni–N–C catalyst showed the optimal ORR property with the half-wave potential ( $E_{1/2}$ ) of 0.938 V (vs RHE), which is better than those of the commercial Pt/C (0.862 V), N–C (0.79 V), Ni–N–C-0.06 (0.893 V), Ni–N–C-0.08 (0.907 V), and Ni–N–C-0.12 (0.884 V) (Figures S15–S17, Supporting Information). These results indicated that with the increase of Ni content, the catalytic activity gradually enhanced, revealing the formation of Ni–N<sub>4</sub> active sites could effectively improve their ORR activities. However, the  $E_{1/2}$  began to decrease when the molar ratio of Ni<sup>2+</sup> was 0.12. This mainly due to the excessive Ni would lead to partial collapse of the polyhedron framework of ZIF-8, thus affecting the ORR electrochemical

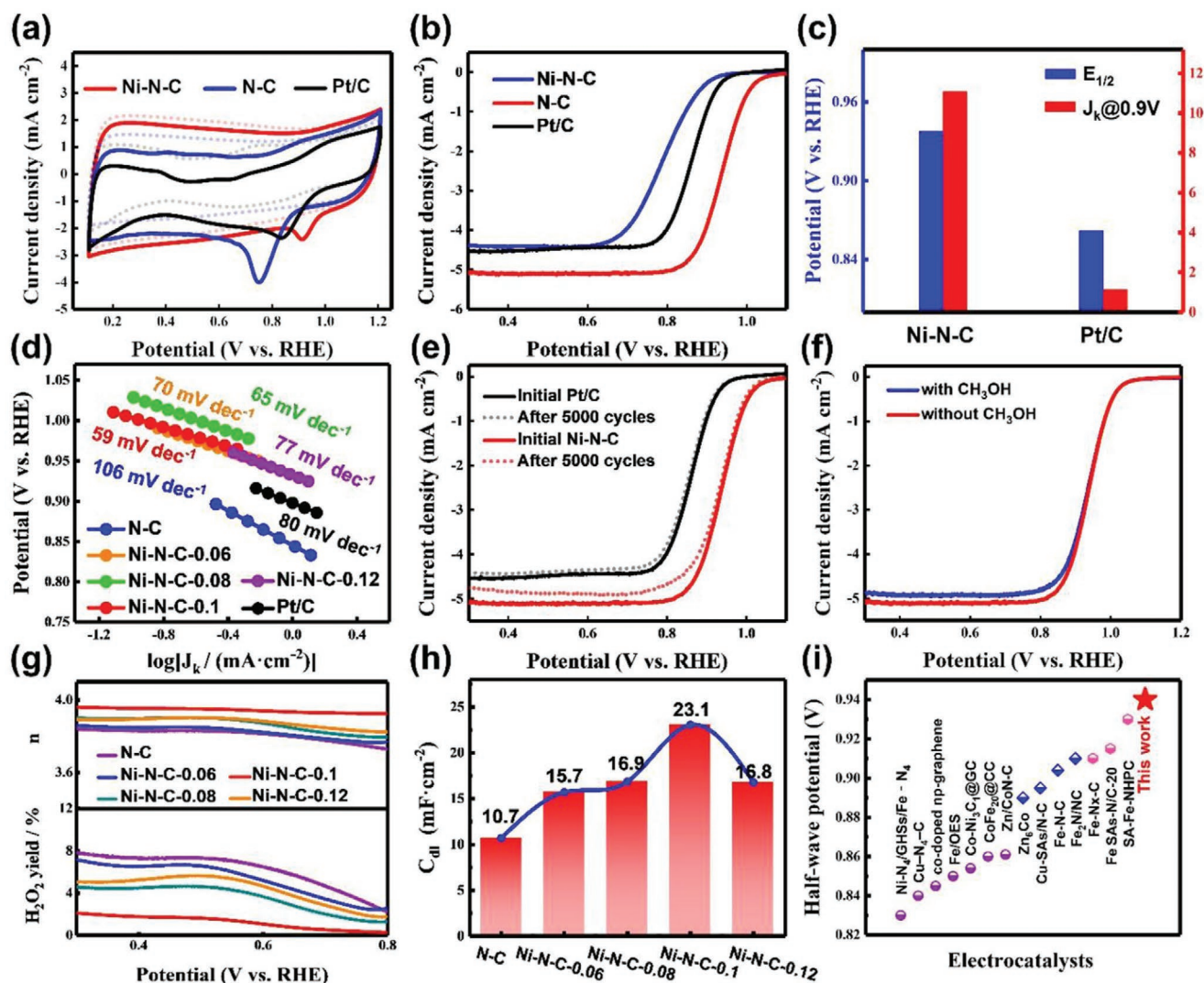


**Figure 3.** a) CV and b) LSV curves measured in O<sub>2</sub> saturated 0.1 M KOH. c) Kinetic current density ( $J_k@0.9V$ ) and  $E_{1/2}$  of Ni-N-C and 20% Pt/C. d) Tafel plots of the obtained Ni-N-C and the references. e) Stability test, f) LSV curves of Ni-N-C-0.1 in O<sub>2</sub>-saturated 0.1 M KOH with 3 M CH<sub>3</sub>OH. g) Peroxide yield and number of transferred electrons of the obtained Ni-N-C and the references. h)  $C_{dl}$  values of Ni-N-C samples. i) Comparisons of ORR performance for the M-N-C catalysts reported in literatures.

performance (Figure S1, Supporting Information). Meanwhile, the influence of the carbonization temperature (800–1000 °C) on ORR properties had also been explored in Figure S18 (Supporting Information). The Ni-N-C treated at 1000 °C demonstrated the optimal ORR performance ( $E_{1/2} = 0.938V$ ). Simultaneously, the kinetic current density analysis showed that the Ni-N-C was 11.09 mA cm<sup>-2</sup>@0.9 V, far exceeded than that of the commercial Pt/C (1.13 mA cm<sup>-2</sup>@0.9 V) (Figure 3c and Figure S19, Supporting Information), which is 9.8 times higher than that of Pt/C. Furthermore, the Tafel slope of Ni-N-C was 59 mV dec<sup>-1</sup>, significantly lower than those of the N-C (106 mV dec<sup>-1</sup>), Ni-N-C-0.12 (77 mV dec<sup>-1</sup>), Ni-N-C-0.06 (70 mV dec<sup>-1</sup>), Ni-N-C-0.08 (65 mV dec<sup>-1</sup>), and the commercial Pt/C catalyst (80 mV dec<sup>-1</sup>), demonstrating the enhanced kinetics (Figure 3d).<sup>[18]</sup> In addition, the  $E_{1/2}$  showed little decay after 5000 potential cycles and the long-term chronoamperometric tests indicated that the high durability for Ni-N-C as

the ORR catalyst (Figure 3e; Figures S20 and S21 and Table S5, Supporting Information). After CV durability test, Ni-N-C kept the dodecahedral structure of ZIF-8 (Figure S22, Supporting Information) and Ni single atom could be found in carbon matrix as shown in Figures S23 and S24 (Supporting Information). Furthermore, XPS results showed that after 3000 and 4000 CV cycles, Ni atoms still existed in the carbon framework as single atoms without agglomeration or oxidation (Figure S25, Supporting Information). Moreover, the Ni-N-C was also measured in O<sub>2</sub>-saturated 0.1 KOH with 3 M CH<sub>3</sub>OH. Linear sweep voltammetry (LSV) curves showed that the presence of methanol had no effect on the oxygen reduction performance in Figure 3f, indicating that the Ni-N-C had strong resistance to methanol poisoning. The electron transfer number showed that Ni-N-C preferentially adopted the four-electron oxygen reduction process. At the same time, the H<sub>2</sub>O<sub>2</sub> yield of Ni-N-C was less than 5%, indicating that H<sub>2</sub>O was the main

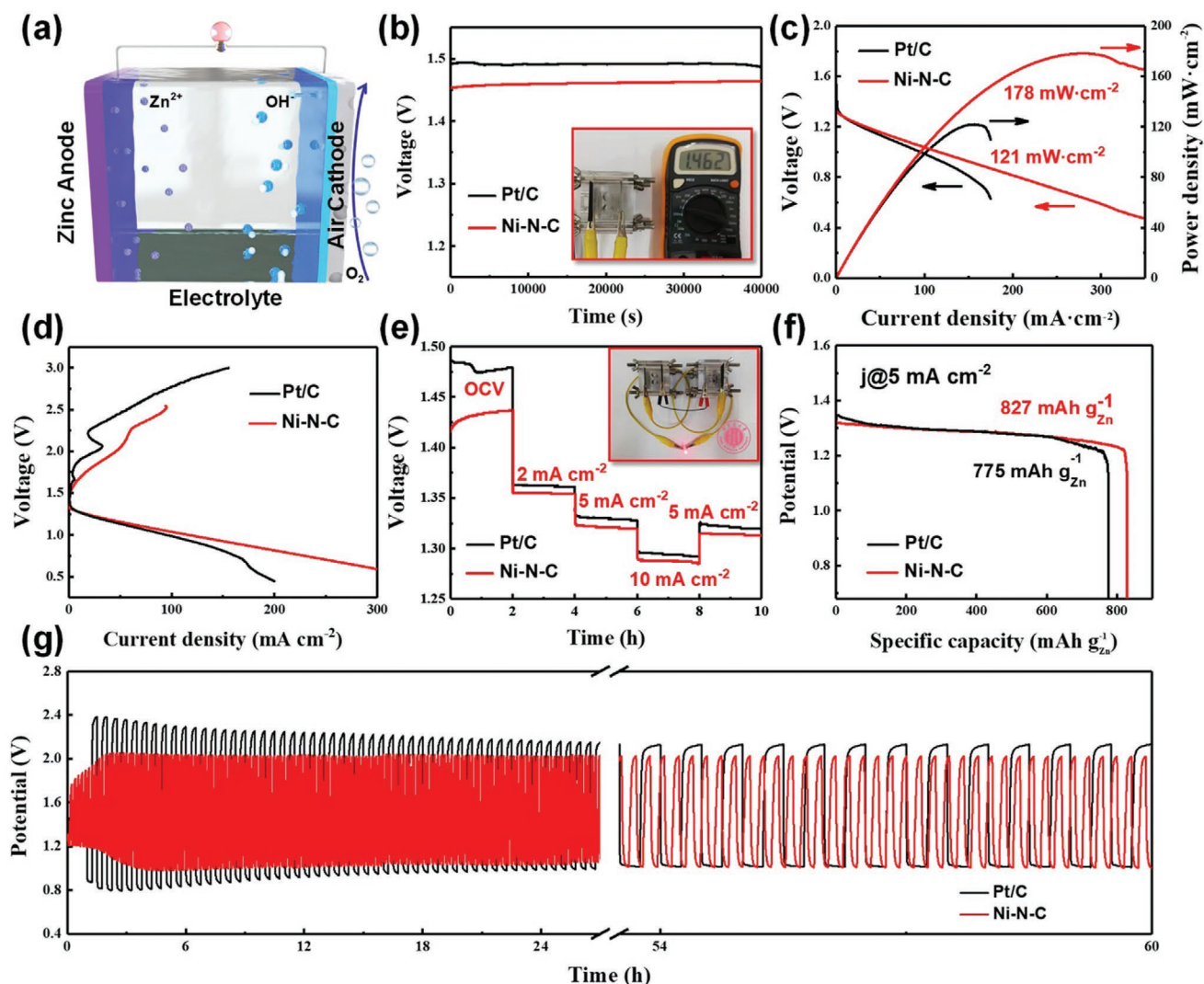


**Figure 4.** a) Schematic diagram of the Zn-air battery, b) open-circuit voltage curves of the catalysts, c) polarization and power density curves, d) discharge/charge curves, e) galvanostatic discharge voltage platform curves of the Ni-N-C electrode at different current densities, a LED light was powered by two cells in the inset, f) specific capacity, and g) discharge/charge cycling curves of Ni-N-C and Pt/C at  $5 \text{ mA cm}^{-2}$ .

oxygen reduction product (Figure 3g).<sup>[19]</sup> Double-layer capacitance ( $C_{dl}$ ) was selected to assess the electrochemical active surface area (ECSA), and the  $C_{dl}$  value was  $23.1 \text{ mF cm}^{-2}$  for Ni-N-C (Figure 3h; Figures S26 and S27, Supporting Information). The above results indicated the larger active surface area and the better catalytic performance for Ni-N-C.<sup>[20]</sup> And the Ni-N-C exhibited the optimal ORR property compared with other M-N-C catalysts reported recently (Figure 3i). Detailed comparisons for ORR catalytic performance were summarized in Table S6 (Supporting Information).

The Ni-N-C sample was used to assemble a Zn-air battery in a  $6.0 \text{ M KOH}$  electrolyte to assess its practical application (Figure 4a). Open-circuit voltages of the Ni-N-C and the commercial Pt/C catalyst were  $1.462$  and  $1.495 \text{ V}$ , respectively (Figure 4b). The curves of Ni-N-C maintain long-term stability after  $40\,000 \text{ s}$  at  $1.462 \text{ V}$ . The optimal power density of the Ni-N-C was  $178 \text{ mW cm}^{-2}$ , which quite surpassed the commercial Pt/C catalyst ( $121 \text{ mW cm}^{-2}$ , Figure 4c). And the

smaller polarization of Ni-N-C indicated better performance at high current density for the Zn-air battery (Figure 4d). At the same time, a small charge-discharge (CD) voltage gap was detected, and the discharge voltage plateaus were  $1.35$ ,  $1.32$ ,  $1.29$ , and  $1.32 \text{ V}$  at  $2$ ,  $5$ ,  $10$ , and  $5 \text{ mA cm}^{-2}$ , respectively, implying that the Ni-N-C had better reversibility and operated at various current densities and processes (Figure 4e).<sup>[20]</sup> A LED light could be powered by two batteries connected in series in Figure 4e. As can be seen from Figure 4f, the specific capacity of the battery assembled by Ni-N-C was estimated to be  $827 \text{ mAh g}_{\text{Zn}}^{-1}$  at the discharge density of  $5 \text{ mA cm}^{-2}$ , much higher than that of the commercial Pt/C ( $775 \text{ mAh g}_{\text{Zn}}^{-1}$ ) and the other catalysts reported recently (Table S7, Supporting Information). The galvanostatic discharge and charge tests were selected to investigate cycling stability of the assembled cells at a current density of  $5 \text{ mA cm}^{-2}$ . In Figure 4g, the Ni-N-C electrode exhibited an outstanding charge-discharge cycling stability for  $60 \text{ h}$  without any significant drop in performance. The

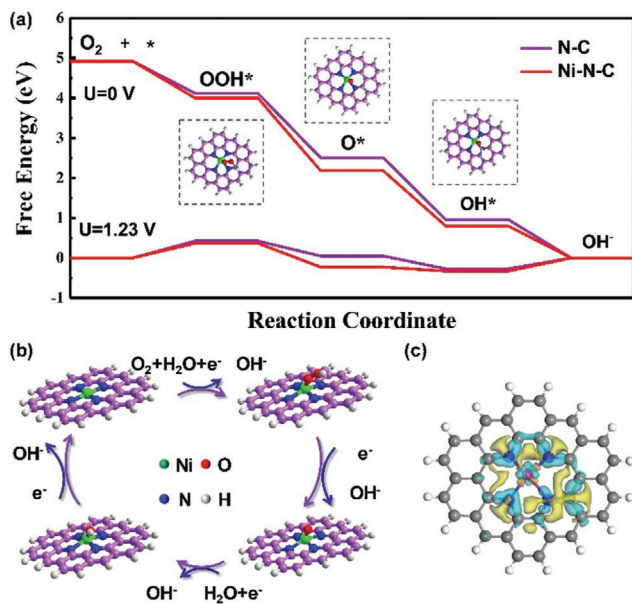
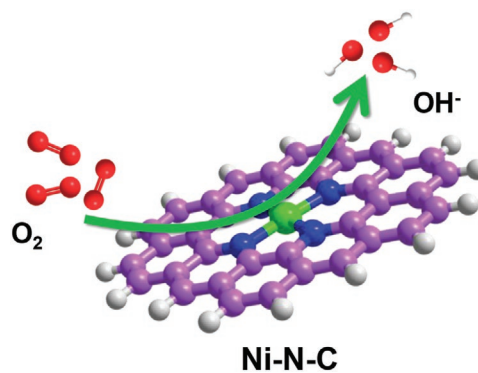


**Figure 5.** a) Free energy diagrams for ORR obtained at zero potential ( $U = 0$  V), working potential, and equilibrium potential ( $U = 1.23$  V) on N-C and Ni-N-C. b) Reaction scheme with the intermediates in the ORR process on Ni-N-C. c) Calculated charge density differences for Ni-N-C.

above results indicated that the Ni-N-C based zinc-air battery had outstanding rechargeable property, long-term stability, and excellent compressibility.

DFT calculations had been implemented to further study the ORR mechanism for the Ni-N<sub>4</sub>-C<sub>10</sub> active center. The obtained structures of Ni-N-C and N-C were constructed in this work. The adsorption free energy of OH\* ( $\Delta G_{\text{OH}^*}$ ) on Ni-N<sub>4</sub>-C<sub>10</sub> could be verified based on the Gibbs free energy diagram for the Ni-N<sub>4</sub>-C<sub>10</sub> site at a potential of 0.0–1.23 V. At the standard ORR potential ( $U = 1.23$  V), some of the basic reactions at active centers were exothermic in **Figure 5a**. The structure of N-C required an energy barrier of 0.425 eV to actuate the first electron transfer step ( $\text{O}_2 + \text{H}_2\text{O} + \text{e}^- + * \rightarrow * \text{OOH} + \text{OH}^-$ ). However, the energy barrier of the first electron transfer step was further decreased to 0.369 eV for the Ni-N-C. Furthermore, the largest energy barrier was the second electron transfer step with the  $\Delta G = 0.597$  eV ( $* \text{OOH} + \text{e}^- \rightarrow * \text{O} + \text{OH}^-$ ), confirming rate-determining step (RDS). For N-C, the RDS was the first electron transfer step with  $\Delta G = 0.425$  eV, demonstrating faster kinetic performance of ORR on Ni-N-C. Structure of reaction intermediate both N-C and Ni-N-C were represented in Figure S31 (Supporting Information). In alkaline solution, the ORR is usually thought to occur in the following steps



**Scheme 1.** Schematic illustration for the enhancement of the ORR performance over Ni-N-C.

where \* represents the adsorption sites. In general, the ORR properties are intently correlated to the intermediates, such as OOH\*, O\*, and OH\*. Figure 5b showed the geometric structures of the intermediates and plausible catalysis mechanism. The density of states (DOS) was further studied, owing to the d-band center is extremely related with the metal-adsorbate interaction.<sup>[22]</sup> The Ni-N-C (-2.25 eV) presented a lower d-band center, indicating that the declined absorption energy of ORR intermediates (Figure S32, Supporting Information). The calculated projected density of states (PDOS) results of Ni-N-C and N-C in Figure S33 (Supporting information) show that the Ni-N-C has the highest density states near the Fermi level. The charge density difference diagrams expressly indicated the intensive charge transfer arising in the Ni-N-C coordination center (Figure 5c and Figure S34, Supporting Information). It means that Ni-N-C has a higher charge density, faster electrons transfer, and better ORR catalytic activity than N-C. The systematic ORR processes of Ni-N-C as cathodic catalysts have been presented in **Scheme 1**.<sup>[23]</sup> The existence of mesopores in the Ni-N-C accelerated the mass transfer of oxygen and the elimination of products, which was beneficial to improve the oxygen reduction performance. At the same time, the lower d-band center of Ni-N-C lead to the reaction intermediate desorbed easily from the active sites, thereby improving the oxygen reduction activity.

At the same time, the lower d-band center of Ni-N-C lead to the reaction intermediate desorbed easily from the active sites, thereby improving the oxygen reduction activity. It is obvious that the outstanding ORR property of Ni-N-C could be ascribed to the following aspects: a) Abundant mesopores in the Ni-N-C were beneficial to mass transfer during ORR process and enhanced ORR catalytic performance. b) Ni-N-C had a lower d-band center (-2.25 eV), indicating that the Ni metal center had a weaker O desorption energy, which accelerated the reaction between the active site and the intermediate, thereby improving the ORR performance. c) Because the abundant mesopores and lower d-band center of Ni-N<sub>4</sub>, the efficiency of the chemical conversion between nickel single-atom sites and adsorbates was improved, thus the synergistic coupling effect of pore structure and Ni-N<sub>4</sub> active site could enhance the catalytic performance of Ni-N-C in alkaline solution (Scheme 1). The above results demonstrated

the Ni–N–C catalyst with the outstanding ORR performance, indicating it is expected as an efficient catalyst for future practical applications.

### 3. Conclusion

In summary, a Ni–N–C catalyst with atomically dispersed Ni–N–C active sites had been prepared by a facile method. Owing to the Ni–N<sub>4</sub> coordination structure, the as-developed Ni–N–C manifests an outstanding ORR activity, as demonstrated by an ultrahigh half-wave potential of 0.938 V, which is currently the best performance among Ni-based single-atoms catalysts. DFT calculation results indicated that the Ni–N–C active sites had higher charge density and faster electron transport efficiency, which could significantly improve the ORR performance. This work offered a facile method to prepare Ni-based single-atom electrocatalyst with outstanding ORR performance, and further studied the intrinsic mechanism of single-atom catalyst under alkaline conditions.

### Supporting Information

Supporting Information is available from the Wiley Online Library or from the author.

### Acknowledgements

S.Z., H.X., and W.-I.L. contributed equally to this work. This project was financially supported by the National Natural Science Foundation of China (21666023, 51872115, 21701168), The financial support by National Key R&D Program of China (2020YFA0406101), Natural Science Foundation of Inner Mongolia Autonomous Region of China (2021ZD11, 2019BS02015), Program for Young Talents of Science and Technology in Universities of Inner Mongolia Autonomous Region (NJYT-19-A01), Dalian high level talent innovation project (2019RQ063), and supported by the 111 Project (D20033). The authors gratefully acknowledge BL14W1 beamline of Shanghai Synchrotron Radiation Facility (SSRF) Shanghai, China for providing the beam time.

### Conflict of Interest

The authors declare no conflict of interest.

### Data Availability Statement

Research data are not shared.

### Keywords

electrocatalysis, hierarchical porous carbon framework, oxygen reduction reaction, single-atom catalysts

Received: April 11, 2021  
Revised: June 11, 2021  
Published online: July 23, 2021

- [1] a) H. A. Gasteiger, N. M. Markovic, *Science* **2009**, 324, 48; b) Z. W. Seh, J. Kibsgaard, C. F. Dickens, I. Chorkendorff, J. K. Nørskov, T. F. Jaramillo, *Science* **2017**, 355, eaad4998; c) M. K. Debe, *Nature* **2012**, 486, 43.
- [2] a) J. R. Varcoe, R. C. T. Slade, *Fuel Cells* **2005**, 5, 187; b) O. Antoine, Y. Bultel, R. Durand, *J. Electroanal. Chem.* **2001**, 499, 85.
- [3] a) J. Wu, H. Yang, *Acc. Chem. Res.* **2013**, 46, 1848; b) Y. Bing, H. Liu, L. Zhang, D. Ghosh, J. Zhang, *Chem. Soc. Rev.* **2010**, 39, 2184; c) K. Strickland, E. Miner, Q. Jia, U. Tylus, N. Ramaswamy, W. Liang, M. T. Sougrati, F. Jaouen, S. Mukerjee, *Nat. Commun.* **2015**, 6, 1130; d) Y. Mu, D. Wang, X. D. Meng, J. Pan, S. D. Han, Z. Z. Xue, *Cryst. Growth Des.* **2020**, 20, 1130.
- [4] a) G. Wu, P. Zelenay, *Acc. Chem. Res.* **2013**, 46, 1878; b) J. D. Pelletier, J. M. Basset, *Acc. Chem. Res.* **2016**, 49, 664; c) J. M. Thomas, R. Raja, D. W. Lewis, *Angew. Chem., Int. Ed.* **2005**, 44, 6456.
- [5] a) X. Tian, X. F. Lu, B. Y. Xia, X. W. Lou, *Joule* **2020**, 4, 45; b) J. Wang, Z. Li, Y. Wu, Y. Li, *Adv. Mater.* **2018**, 30, 1801649; c) J. B. Wu, L. K. Xiong, B. T. Zhao, M. L. Liu, L. Huang, *Small Methods* **2020**, 4, 1900540.
- [6] a) C.-C. Hou, H.-F. Wang, C. Li, Q. Xu, *Energy Environ. Sci.* **2020**, 13, 1658; b) B. Zhu, D. Xia, R. Zou, *Coord. Chem. Rev.* **2018**, 376, 430.
- [7] a) L. Jiao, H.-L. Jiang, *Chem* **2019**, 5, 786; b) P. Yin, T. Yao, Y. Wu, L. Zheng, Y. Lin, W. Liu, H. Ju, J. Zhu, X. Hong, Z. Deng, G. Zhou, S. Wei, Y. Li, *Angew. Chem., Int. Ed.* **2016**, 55, 10800; c) Y. Chen, S. Ji, S. Zhao, W. Chen, J. Dong, W. C. Cheong, R. Shen, X. Wen, L. Zheng, A. I. Rykov, S. Cai, H. Tang, Z. Zhuang, C. Chen, Q. Peng, D. Wang, Y. Li, *Nat. Commun.* **2018**, 9, 5422; d) Y. Jing, Y. Cheng, L. Wang, Y. Liu, B. Yu, C. Yang, *Chem. Eng. J.* **2020**, 397, 125539; e) J. Long, R. Li, X. Gou, *Catal. Commun.* **2017**, 95, 31; f) V. Priya K, M. Thomas, R. Illathvalappil, S. K, S. Kurungot, B. N. Nair, A. P. Mohamed, G. M. Anilkumar, T. Yamaguchi, U. S. Hareesh, *New J. Chem.* **2020**, 44, 12343.
- [8] a) H. Peng, F. Liu, X. Liu, S. Liao, C. You, X. Tian, H. Nan, F. Luo, H. Song, Z. Fu, P. Huang, *ACS Catal.* **2014**, 4, 3797; b) C. Zhu, Q. Shi, B. Z. Xu, S. Fu, G. Wan, C. Yang, S. Yao, J. Song, H. Zhou, D. Du, S. P. Beckman, D. Su, Y. Lin, *Adv. Energy Mater.* **2018**, 8, 1801956; c) J. Masa, A. Zhao, W. Xia, M. Muhler, W. Schuhmann, *Electrochim. Acta* **2014**, 128, 271; d) F. Calle-Vallejo, J. I. Martinez, J. Rossmeisl, *Phys. Chem. Chem. Phys.* **2011**, 13, 15639; e) L. Osmieri, A. H. A. M. Videla, P. Ocón, S. Specchia, *J. Phys. Chem. C* **2017**, 121, 17796.
- [9] Y. Zheng, D.-S. Yang, J. M. Kweun, C. Li, K. Tan, F. Kong, C. Liang, Y. J. Chabal, Y. Y. Kim, M. Cho, J.-S. Yu, K. Cho, *Nano Energy* **2016**, 30, 443.
- [10] X. Li, H. Rong, J. Zhang, D. Wang, Y. Li, *Nano Res.* **2020**, 13, 1842.
- [11] Y. Pan, S. Liu, K. Sun, X. Chen, B. Wang, K. Wu, X. Cao, W. C. Cheong, R. Shen, A. Han, Z. Chen, L. Zheng, J. Luo, Y. Lin, Y. Liu, D. Wang, Q. Peng, Q. Zhang, C. Chen, Y. Li, *Angew. Chem., Int. Ed.* **2018**, 57, 8614.
- [12] R. Jiang, L. Li, T. Sheng, G. Hu, Y. Chen, L. Wang, *J. Am. Chem. Soc.* **2018**, 140, 11594.
- [13] a) M. Xiao, L. Gao, Y. Wang, X. Wang, J. Zhu, Z. Jin, C. Liu, H. Chen, G. Li, J. Ge, Q. He, Z. Wu, Z. Chen, W. Xing, *J. Am. Chem. Soc.* **2019**, 141, 19800; b) H. W. Liang, X. Zhuang, S. Bruller, X. Feng, K. Mullen, *Nat. Commun.* **2014**, 5, 4973.
- [14] a) D. Yan, Y. Li, J. Huo, R. Chen, L. Dai, S. Wang, *Adv. Mater.* **2017**, 29, 1606459; b) L. Jiao, R. Zhang, G. Wan, W. Yang, X. Wan, H. Zhou, J. Shui, S. H. Yu, H. L. Jiang, *Nat. Commun.* **2020**, 11, 2831.
- [15] B. Y. Xia, Y. Yan, N. Li, H. B. Wu, X. W. Lou, X. Wang, *Nat. Energy* **2016**, 1, 15006.
- [16] Z. Zhu, H. Yin, Y. Wang, C. H. Chuang, L. Xing, M. Dong, Y. R. Lu, G. Casillas-Garcia, Y. Zheng, S. Chen, Y. Dou, P. Liu, Q. Cheng, H. Zhao, *Adv. Mater.* **2020**, 32, 2004670.
- [17] b) S. Ding, Y. Guo, M. J. Hülsey, B. Zhang, H. Asakura, L. Liu, Y. Han, M. Gao, J.-Y. Hasegawa, B. Qiao, T. Zhang, N. Yan, *Chem*

- 2019, 5, 3207; b) H. B. Zhang, L. Yu, T. Chen, W. Zhou, X. W. Lou, *Adv. Funct. Mater.* **2018**, 28, 1807086.
- [18] L. Yang, D. Cheng, H. Xu, X. Zeng, X. Wan, J. Shui, Z. Xiang, D. Cao, *Proc. Natl. Acad. Sci. USA* **2018**, 115, 6626.
- [19] H. Zhang, H. T. Chung, D. A. Cullen, S. Wagner, U. I. Kramm, K. L. More, P. Zelenay, G. Wu, *Energy Environ. Sci.* **2019**, 12, 2548.
- [20] Y. Mun, S. Lee, K. Kim, S. Kim, S. Lee, J. W. Han, J. Lee, *J. Am. Chem. Soc.* **2019**, 141, 6254.
- [21] K. Wu, L. Zhang, Y. Yuan, L. Zhong, Z. Chen, X. Chi, H. Lu, Z. Chen, R. Zou, T. Li, C. Jiang, Y. Chen, X. Peng, J. Lu, *Adv. Mater.* **2020**, 32, 2002292.
- [22] a) J. K. Nørskov, J. Rossmeisl, A. Logadottir, L. Lindqvist, J. R. Kitchin, T. Bligaard, H. Jonsson, *J. Phys. Chem. B* **2004**, 108, 17886; b) V. Stamenkovic, B. S. Mun, K. J. J. Mayrhofer, P. N. Ross, N. M. Markovic, J. Rossmeisl, J. Greeley, J. K. Nørskov, *Angew. Chem.* **2006**, 118, 2963; c) L. A. Kibler, A. M. El-Aziz, R. Hoyer, D. M. Kolb, *Angew. Chem., Int. Ed.* **2005**, 44, 2080.
- [23] a) X. M. Ge, A. Sumboja, D. Wu, T. An, B. Li, F. W. T. Goh, T. S. A. Hor, Y. Zong, Z. L. Liu, *ACS Catal.* **2015**, 5, 4643; b) H. A. Firouzjaie, W. E. Mustain, *ACS Catal.* **2019**, 10, 225.